

Quantum-informed plasmonics for strong coupling: the role of electron spill-out

Ida Juliane Bundgaard,¹ Christian Nicolaisen Hansen,¹ P. Elli Stamatopoulou¹ ¹ and Christos Tserkezis^{1,*} 

¹*POLIMA—Center for Polariton-driven Light-Matter Interactions,
University of Southern Denmark, Campusvej 55, DK-5230 Odense M, Denmark*

(Dated: November 13, 2023)

The effect of nonlocality on the optical response of metals lies at the forefront of research in nanoscale physics and, in particular, quantum plasmonics. In alkali metals, nonlocality manifests predominantly as electron density spill-out at the metal boundary, and as surface-enabled Landau damping. For an accurate description of plasmonic modes, these effects need to be taken into account in the theoretical modelling of the material. The resulting modal frequency shifts and broadening become particularly relevant when dealing with the strong interaction between plasmons and excitons, where hybrid modes emerge and the way they are affected can reflect modifications of the coupling strength. Both nonlocal phenomena can be incorporated in the classical local theory by applying a surface-response formalism embodied by the Feibelman parameters. Here, we implement surface-response corrections in Mie theory to study the optical response of spherical plasmonic–excitonic composites in core–shell configurations. We investigate sodium, a jellium metal dominated by spill-out, for which it has been anticipated that nonlocal corrections should lead to an observable change in the coupling strength, appearing as a modification of the width of the mode splitting. We show that, contrary to expectations, the influence of nonlocality on the anticrossing is minimal, thus validating the accuracy of the local response approximation in strong-coupling photonics.

I. INTRODUCTION

Plasmonics deals with the collective oscillations of free electrons in the bulk or on the surface of metallic structures due to an external electromagnetic (EM) excitation [1–4]. The quasiparticles of plasma oscillations on the surface of metallic nanoparticles (NPs), called localized surface plasmons (LSPs), are known for their ability to strongly enhance and confine the incident light in subwavelength volumes [5]. Owing to these properties, plasmonic NPs constitute ideal platforms for various applications, such as in optical communications [6], photovoltaics [7] and sensors [8]. To increase the practical benefit from such systems, it has long been a trend to minimize the dimensions of the NPs involved, in order to obtain a more dramatic confinement of light. This goal is achievable as modern technologies allow the fabrication and characterisation of metallic structures of ever decreasing nanometric dimensions. At the extreme nanoscale of sizes $\lesssim 10$ nm, the local response approximation (LRA), based on the Drude model [9, 10], or on the experimentally measured permittivity of the bulk metal, can no longer accurately predict the optical response of the system.

Quantum-informed plasmonics [11] aims to incorporate nonlocal effects of quantum-mechanical origin into the description of the system [12], including screening, Landau damping, and electron spill-out [13]. Screening, in the case of a metallic NP, refers to the free electrons experiencing a smaller restoring force, due to charge shielding from the bound electrons in low-lying bands, leading to the electron density spilling inwards at the assumed metal boundary [14]. Landau damping describes the decay of the plasma oscillations into electron–hole pairs, and is enhanced in small NPs due to collisions of conduction electrons with the metal boundary [15, 16]. Electron

spill-out describes the fact that the electron density does not terminate abruptly, but rather has a smoother profile, that spills out of the formal boundary of the metal [17]. One of the most widely used nonlocal models that takes screening into account is the Hydrodynamic Drude model (HDM) [18–20]; by extending HDM to the generalized nonlocal optical response (GNOR) model [21], we can additionally reproduce Landau damping. However, both HDM and GNOR typically rely on a hard-wall boundary condition, which assumes that the electron density is zero beyond the formal boundary of the NP [22, 23], meaning that electron spill-out is overlooked; self-consistent variants of HDM that can take this effect into account have been proposed, but they remain computationally heavy [24–26].

Whether screening or spill-out is the dominant mechanism determining the optical response of the metal depends on its work function. In alkali metals, that are characterized by low work functions, spill-out is most significant [27–29]. An elegant way to incorporate this effect in the description of the system is offered by the Feibelman formalism, in which nonlocality is encompassed by means of surface-response functions [30]. This framework invokes new boundary conditions at the air–metal interface using the surface-response parameters d_{\perp} and d_{\parallel} , which correspond to an induced surface charge and current density, respectively [31]. It thus allows the bulk response of the plasmonic material to still be locally modelled, while introducing a discontinuity due to the surface polarization [30]. In general, the d -parameters are complex numbers with dimensions of length; the real parts of the d -parameters express the position of the charge/current centroid, whereas the imaginary parts account for surface-enabled Landau damping [32].

Due to the strong field enhancement and confinement that plasmonic NPs achieve, they are often used as (open)

nanocavities [33], in order to enhance the excitation and emission processes of nearby emitters [34–38]. When a cavity is coupled strongly to an emitter, modal hybridization and reversible energy exchange can occur between the two components [39–42]. One advantage of plasmonic nanocavities is the large control over the plasmonic mode by the modulation of their size, which is enabled by nanofabrication techniques [43]. To achieve high coupling strengths, plasmons are most commonly combined with excitonic materials that sustain collective optical excitations, such as low-dimensional semiconductors or organic dye molecules [44–47]. By tuning the plasmonic mode and reducing the size of the metallic NPs—and thus the mode volume, plasmon–exciton geometries show strong potential for generating wide Rabi splitting, and thus enabling the study of quantum effects at room temperature [48, 49].

The effect of screening and Landau damping in strongly-coupled, composite core–shell NPs consisting of a noble metal and an excitonic material has been studied earlier, within the HDM and GNOR models. In particular, it was found that the width of the Rabi splitting is not affected by such corrections. On the one hand, both hybrid modes shift in energy by the same amount; on the other hand, for such small NPs the increase of the effective mode volume due to Landau damping is typically rather small, and its influence on the anticrossing is counterbalanced by the nonlocal blueshift of the modes [50]. Nevertheless, it was speculated that the situation should be different in cases where spill-out is the dominant quantum effect. In this work, the surface-response formalism (SRF) framework is applied to determine whether electron spill-out indeed affects the coupling strength in NPs consisting of sodium and excitonic components. Specifically, we explore whether it influences the width of the mode anticrossing, when compared to the LRA prediction.

II. RESULTS AND DISCUSSION

In what follows, we study the optical response of core–shell NPs in two different configurations, focusing on corrections pertaining to electron spill-out and Landau damping. Sodium, in which spill-out is non-negligible [51, 52], is the plasmonic material considered throughout the paper, since its simple atomic structure has rendered it the workhorse of theoretical quantum plasmonics [53–55]. Within LRA, sodium is modelled with the simple Drude model, expressing the relative permittivity ε as a function of angular frequency ω as

$$\varepsilon = 1 - \frac{\omega_p^2}{\omega(\omega + i\gamma_p)}, \quad (1)$$

with plasma frequency ω_p and damping rate γ_p , given as $\hbar\omega_p = 5.89132$ eV and $\hbar\gamma_p = 0.1$ eV. From now on, all frequencies will appear normalized to ω_p .

The optical response of the NPs is investigated using Mie theory [56]; the incident, scattered, and internal fields are expanded in a sum of spherical waves of multipolar order ℓ , and the connection between their amplitudes is given by the scattering Mie coefficients $T_{E\ell}$ and $T_{H\ell}$ (where E, H stands for transverse-electric and transverse-magnetic polarization, respectively). The Mie coefficients are straightforward to calculate through the usual pillbox boundary conditions at the particle (medium 1)–environment (medium 2) interface, which, in the absence of surface charges and currents, translate into continuity of the tangential components of the electric and magnetic fields, $\mathbf{E}_{2\parallel} - \mathbf{E}_{1\parallel} = 0$ and $\mathbf{H}_{2\parallel} - \mathbf{H}_{1\parallel} = 0$ [9].

In SRF, the Feibelman d -parameters are introduced in a modified Mie description. These parameters, typically calculated for an infinite flat metal–dielectric interface, are defined as [30]

$$d_{\perp}(\omega) = \frac{\int dx x \rho(x, \omega)}{\int dx \rho(x, \omega)}, \quad d_{\parallel}(\omega) = \frac{\int dx x \partial_x J_y(x, \omega)}{\int dx \partial_x J_y(x, \omega)}, \quad (2)$$

where x is the direction normal to the interface, ρ is the induced charge density, and \mathbf{J} the corresponding current density. They can be incorporated into the boundary conditions of the problem [31],

$$\mathbf{E}_{2\parallel} - \mathbf{E}_{1\parallel} = -d_{\perp} \nabla_{\parallel} (E_{2\perp} - E_{1\perp}), \quad (3a)$$

$$\mathbf{H}_{2\parallel} - \mathbf{H}_{1\parallel} = i\omega d_{\parallel} (\mathbf{D}_{2\parallel} - \mathbf{D}_{1\parallel}) \times \hat{\mathbf{n}}, \quad (3b)$$

where \mathbf{D} is the displacement field, ∇_{\parallel} is the surface nabla operator, \perp denotes the field component normal to the interface, and $\hat{\mathbf{n}}$ the unit vector normal to the interface. It should be noted that the use of Feibelman parameters for curved interfaces imposes requirements on the dimensions of the system. For a spherical particle of radius R , we require $R \gg \ell d_{\perp, \parallel}$ [31]; the applicability of the formalism can further be extended by considering nonlocal Feibelman parameter [57, 58]. The modified Mie coefficients used throughout this paper can be found in the Appendix.

A. Surface Response Formalism for Sodium Nanoparticles

To demonstrate the effect of spill-out on the optical response of plasmonic NPs, we first consider a sodium sphere of radius R_1 embedded in air. Following Ref. [31], the d_{\perp} parameter is given by Lorentzian fitting to time-dependent density-functional theory calculations, where sodium was treated as a jellium of Wigner-Seitz radius $r_s = 4$ [59]. A plot of the real and imaginary part of d_{\perp} is presented in Fig. 1a. We set $d_{\parallel} = 0$, which is appropriate for charge-neutral surfaces [30, 32].

Figs. 1b and c show the extinction cross sections of a sodium NP surrounded by air, for varying radii R_1 , calculated within LRA and SRF, respectively. Up to a

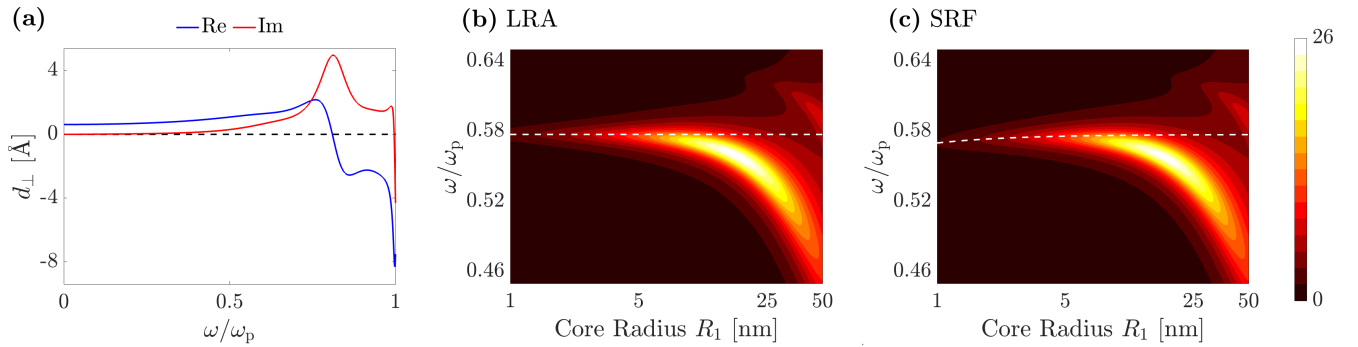


FIG. 1. (a) Real (blue line) and imaginary (red line) part of the perpendicular Feibelman parameter d_{\perp} for a flat sodium–air interface [31]. (b), (c) Contour maps of the extinction cross section (in logarithmic scale), normalized to the geometric cross section πR_1^2 , for varying radius of a spherical sodium NP, obtained with (b) LRA and (c) SRF, sharing a common color scale. The frequency of the incident light ω is normalized to the plasma frequency ω_p of sodium in all panels. The white dashed line in (b) marks the quasistatic frequency $\omega_p/\sqrt{3}$; in (c), the white dashed line gives the corresponding frequency according to Eq. (4).

radius of around $R_1 = 25$ nm, the only mode contributing to the extinction spectra for both LRA and SRF is the electric dipolar (ED) LSP. As the radius is decreased, the ED resonance energy in LRA converges to the quasistatic limit $\omega_1^{(cl)}/\omega_p = 1/\sqrt{3} \simeq 0.58$. This value is indicated with the dashed white line in Fig. 1b, and captures the absence of retardation of the free electrons in the NP, which experience the incident field as spatially constant. In SRF, in which the electron density varies over the NP volume, and thus the field that the NP experiences cannot be assumed constant, the ED resonance energy deviates from the local quasistatic limit and follows the relation

$$\omega_1^{(a)} = \omega_1^{(cl)} \sqrt{1 - 2d_{\perp}/R_1}, \quad (4)$$

as indicated by the dashed white line in Fig. 1c. As the NP dimensions increase, and retardation becomes important, higher multipole contributions emerge. The electric quadrupolar (EQ) mode is seen in Figs. 1b and c at approximately $0.61\omega_p$. The effect of spill-out and Landau damping is most prominent for NP radii below 5 nm, manifested in SRF as a red-shift and a broadening of the plasmon resonance in the extinction spectrum, compared to the local model.

B. Sodium Core with an Excitonic Shell

Having now established the corrections to the plasmonic core alone, we introduce an excitonic material to obtain strong coupling. Here, we investigate a spherical sodium core of varying radius R_1 , encapsulated in an excitonic shell with a fixed thickness $W = 2$ nm, embedded in air. The excitonic shell is modelled with the Drude-Lorentz model,

$$\epsilon_{\text{exc}}(\omega) = 1 - \frac{f\omega_{\text{exc}}}{\omega^2 - \omega_{\text{exc}}^2 + i\omega\gamma_{\text{exc}}}, \quad (5)$$

with excitonic energy $\hbar\omega_{\text{exc}} = 3.38$ eV, damping rate $\hbar\gamma_{\text{exc}} = 0.06$ eV, and oscillator strength $f = 0.02$ [60]. The scattering Mie coefficients core-shell NP are given by (11) and (12) in the Appendix.

The spectra of the extinction cross section for NPs with $R_1 = 2$ nm and $R_1 = 7.3$ nm sodium core are shown in Fig. 2a and Fig. 2b, respectively. The SRF (LRA) extinction spectrum is given by the red (black) line, with the dashed lines denoting the extinction spectra for the sodium core in the absence of the excitonic shell. All spectra are normalized to the geometric cross section πR^2 , where $R = R_1 + W$ for the core-shell NP, and $R = R_1$ for the sodium core alone. The interaction of the excitonic material with the LSP forms two hybrid modes, as expected from literature [61], with a mixed plasmonic-excitonic character. Their energies are denoted as ω_{\pm} for the lower (–) and upper (+) hybrid mode, respectively. Between the two hybrid modes there is a weak peak at $\omega/\omega_p = 0.57$. This is a geometric resonance of the charge oscillations that matches the excitonic energy of the system, where the plasmonic core and excitonic shell act as a uniform material [61], and it does not participate in the coupling.

For both core radii, the introduction of nonlocal effects through SRF produces a redshift of both hybrid modes compared to the local model, albeit a more significant shift for the upper hybrid mode than for the lower one. Additionally, both modes in the nonlocal model experience broadening compared to the local model, again more significant for the upper hybrid mode. The redshift and damping of the hybrid modes is larger for the smaller core radius of $R_1 = 2$ nm in Fig. 2a, compared to $R_1 = 7.3$ nm in Fig. 2b. This can be explained by the electron spill-out effectively increasing the core radius, allowing for LSPs of longer wavelengths. This, in turn, introduces a detuning of the plasmon energy for SRF compared to LRA, red-shifting the hybrid modes.

To better visualize the trends of the hybrid modes, a

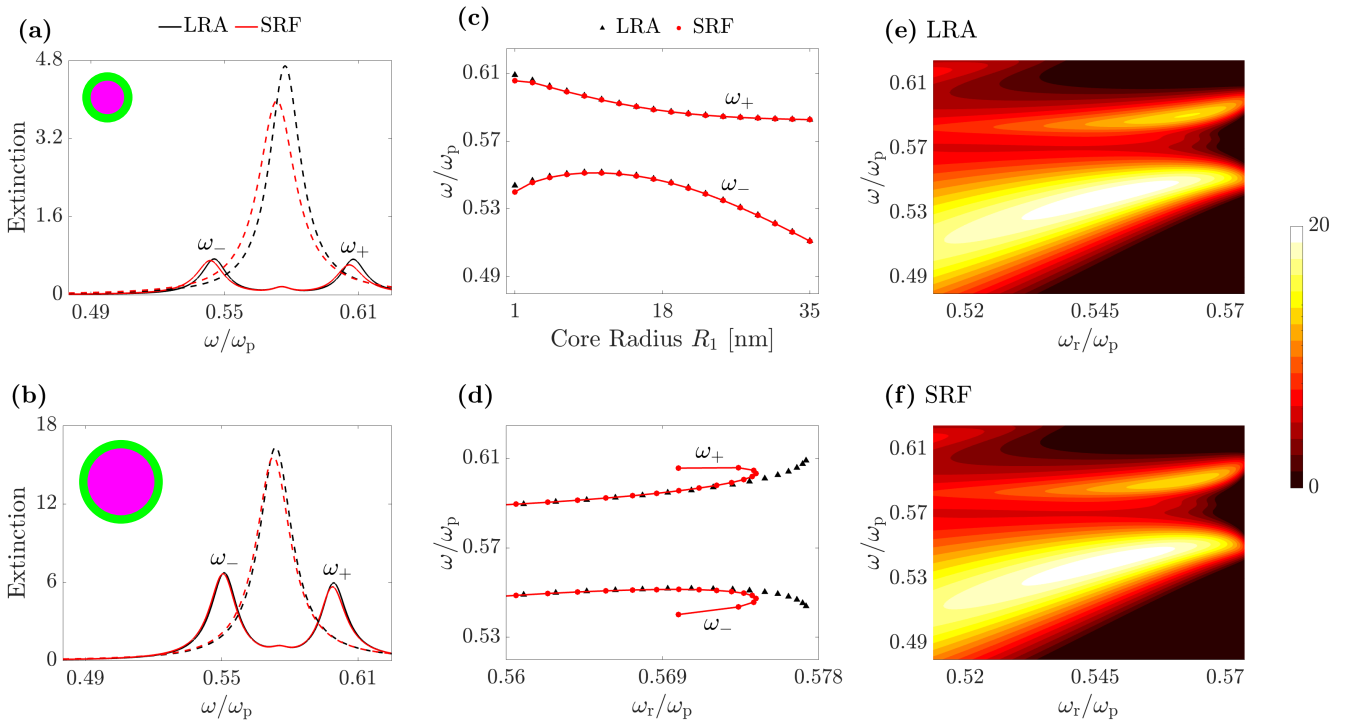


FIG. 2. (a, b) Extinction cross sections, normalized to the geometric cross section πR^2 , for a sodium core of radius (a) 2 nm and (b) 7.3 nm, both with an excitonic shell of 2 nm thickness obtained from SRF (red solid line), compared to LRA (black solid line), showing the two hybrid modes ω_{\pm} . The dashed lines correspond to the sodium core alone. (c, d) Hybrid mode resonance energies within SRF (red dots) and within LRA (black triangles) as a function of (c) the sodium core radius and (d) the sodium core resonance frequency ω_r , normalized to ω_p . The red lines show the trend of the resonance energies in SRF for both hybrid modes compared to LRA (black lines). does not signify an increase in coupling strength but the shift of the uncoupled resonance frequency ω_r . (e, d) Logarithmically scaled extinction contour maps as a function of resonance frequency ω_r for (e) LRA and (f) SRF, sharing a common color scale.

comparison of SRF and LRA is provided in Figs. 2c and d, showing the resonance energies of the hybrid modes as functions of select sodium-core radii and of select sodium-core resonance frequencies ω_r , respectively. The resonance frequency ω_r is given by the LSP of the sodium core in the absence of the excitonic shell for varying R_1 . The radius of the sodium core in Fig. 2c varies from 1 to 35 nm, while the width of the excitonic shell is fixed at 2 nm. We observe that for both hybrid modes, the differences in energy between LRA and SRF hybrid modes are most significant for a decreasing core radius R_1 smaller than about $R_1 \approx 3$ nm. At a 1 nm core radius, which lies at the limits of validity of SRF, the energy difference between LRA and SRF is $0.0035\omega_p$ for the upper mode, and $0.0037\omega_p$ for the lower mode. For LRA, a decreasing radius corresponds to an increase in ω_r . But for SRF, a decrease in core radius only leads to an increase in ω_r up to about $0.574\omega_p$. At around this frequency, referencing Fig. 1b, further decrease in R_1 now leads to a decrease in ω_r . As both peaks of the SRF hybrid modes are redshifted in energy compared to LRA, the energy difference, and thus the coupling strength between the hybrid modes remains practically unaffected in SRF compared to LRA at each core radius.

When considering mode splitting, we commonly address the spectrum where zero detuning between the two modes occurs, namely, where the resonance ω_r of the sodium core matches the resonance of the excitonic shell. Zero detuning in the local model occurs for a core radius of $R_1 = 7.3$ nm, with the energy difference between the hybrid mode peaks found to be $0.048\omega_p$. In the non-local model, zero detuning occurs at a lower core radius than for LRA, at $R_1 = 6.0$ nm, with the energy difference between hybrid modes being $0.051\omega_p$ (≈ 300 meV). Comparing SRF to LRA, this is a difference of $0.0027\omega_p$, with the larger anticrossing occurring in the nonlocal model. With practically no change in the coupling strength from LRA to SRF at each core radius, this change in anticrossing is attributed to the fact that zero detuning occurs for two different radii.

Lastly, to examine the effect of resonance broadening due to Landau damping, we consult the contour plots of Figs. 2e and f, where we plot the extinction cross section of the coupled system as a function of the resonance energy ω_r , in LRA and SRF, respectively. Clearly, no significant broadening can be observed, and the two plots are nearly identical, since SRF reproduces a similar coupling strength. For high frequencies of the incident light and

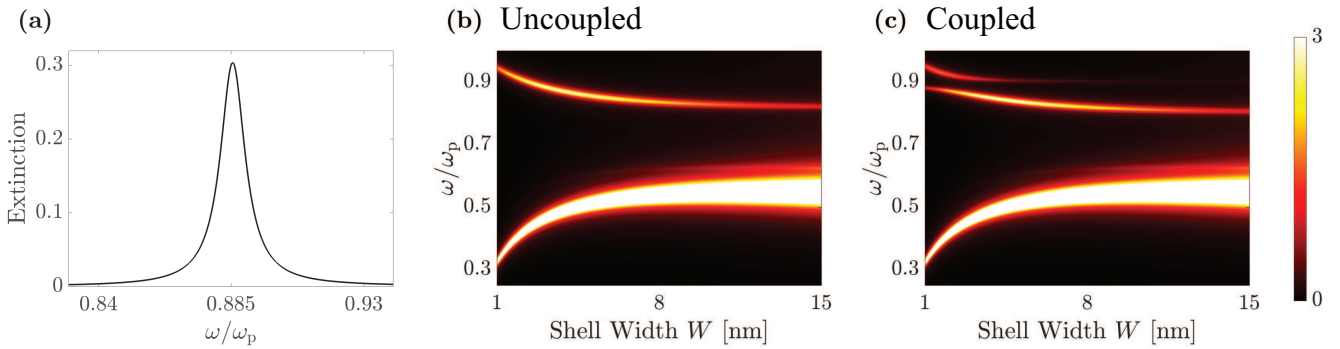


FIG. 3. (a) Extinction cross section of a spherical excitonic core with radius $R_1 = 5$ nm embedded in air. (b, c) Extinction contour maps as a function of shell width for (b) a vacuum core with a radius of 5 nm with a sodium shell, and (c) the combined excitonic core–sodium shell. The color bar is shared for (b) and (c). All results are obtained within LRA.

low resonance frequencies ω_r , we see also the EQ ($\ell = 2$) resonance for the sodium core, which, due to its large detuning to the excitonic energy, does not participate in the coupling.

C. Excitonic Core with a Sodium Shell

We now investigate the inverted geometry, i.e. a spherical excitonic core with a fixed radius $R_1 = 5$ nm, encapsulated in a sodium shell of varying width W , and subsequently varying outer radius $R = R_1 + W$. The excitonic core is now modelled with an excitonic energy of $\hbar\omega_{\text{exc}} = 5.2$ eV ($\omega_{\text{exc}} = 0.88\omega_p$), while all other parameters remain the same as in section II B. Because the new geometry has two plasmonic surfaces, Feibelman corrections must apply on both. The nonlocal scattering Mie coefficients are now given by (13) and (14), while for the inner boundary we use (9) and (10) in the Appendix. When considering the inner boundary of the sodium shell, it should be noted that the spill-out occurs radially towards the centre of the coordinate system. The Feibelman parameters, expressing lengths evaluated with respect to the metal–environment interface, are directionally dependent, with the positive direction previously assumed to be radially outwards. Therefore, the sign of the Feibelman parameter shown in Fig. 1 must be inverted when dealing with the inner boundary of the sodium shell.

Fig. 3a shows the extinction cross section of the excitonic core with a radius of 5 nm, while Fig. 3b shows a contour map of the LRA extinction cross section of a sodium shell thickness W ranging between 1 and 15 nm, in the absence of the excitonic core. The spectrum of the excitonic core is a singular peak at $\omega_{\text{exc}}/\omega_p \simeq 0.88$. The sodium shell has two distinct LSP modes; the higher energy mode is a cavity mode, originating from LSPs at the inner surface of the shell, while the lower mode is the NP mode, originating from the outer surface of the shell [62]. A contour map of the LRA extinction cross section for

the sodium shell in the presence of the excitonic core is presented in Fig. 3c, showing an anticrossing emerging between the cavity mode and the excitonic transition, at the excitonic energy, indicating strong coupling. As the cavity mode is the one participating in the coupling, in what follows we only consider this mode when discussing the effect of the Feibelman corrections.

Figs. 4a and b show the extinction spectrum for the sodium shell with an air or excitonic core, for shell widths $W = 3.14$ nm and $W = 13.0$ nm, respectively. When considering nonlocal effects, the uncoupled cavity mode of the plasmonic shell experiences damping and blueshift compared to the LRA spectrum, though it can be seen that the blueshift is greater for the smaller shell width; the upper hybrid modes on both graphs follow the same trend. Looking at the lower hybrid modes in the two spectra, they both experience damping in SRF compared to LRA, but in Fig. 4b we see a redshift for the lower hybrid mode. The opposite shifts are the result of the nonlocality affecting both the coupling of the cavity mode to the NP mode and the cavity mode alone. For this geometry, the electron spill-out effectively increases the shell width compared to LRA, leading to a spectral redshift of the cavity mode compared to LRA. At the same time, at the inner shell boundary, the electron spill-out effectively decreases the inner radius R_1 of the shell, meaning that the LSPs in the cavity for the SRF model will have shorter wavelengths than those in the LRA model, leading to a blueshift of the SRF cavity mode spectrum compared to LRA. In the quasistatic limit, we find the correction to the electric dipole resonance frequency of the cavity mode to be

$$\omega_{1c}^{(q)} = \omega_{1c}^{(cl)} \sqrt{1 - d_{\perp}/R_1}, \quad (6)$$

where the quasistatic LRA cavity-mode resonance frequency is $\omega_{1c}^{(cl)}/\omega_p = \sqrt{2/3} \simeq 0.82$. These two nonlocal contributions result in an overall blueshift of the lower mode at most shell widths, such as the one shown in Fig. 4a, indicating that the contribution of the correction to the coupling is more significant. However, at the

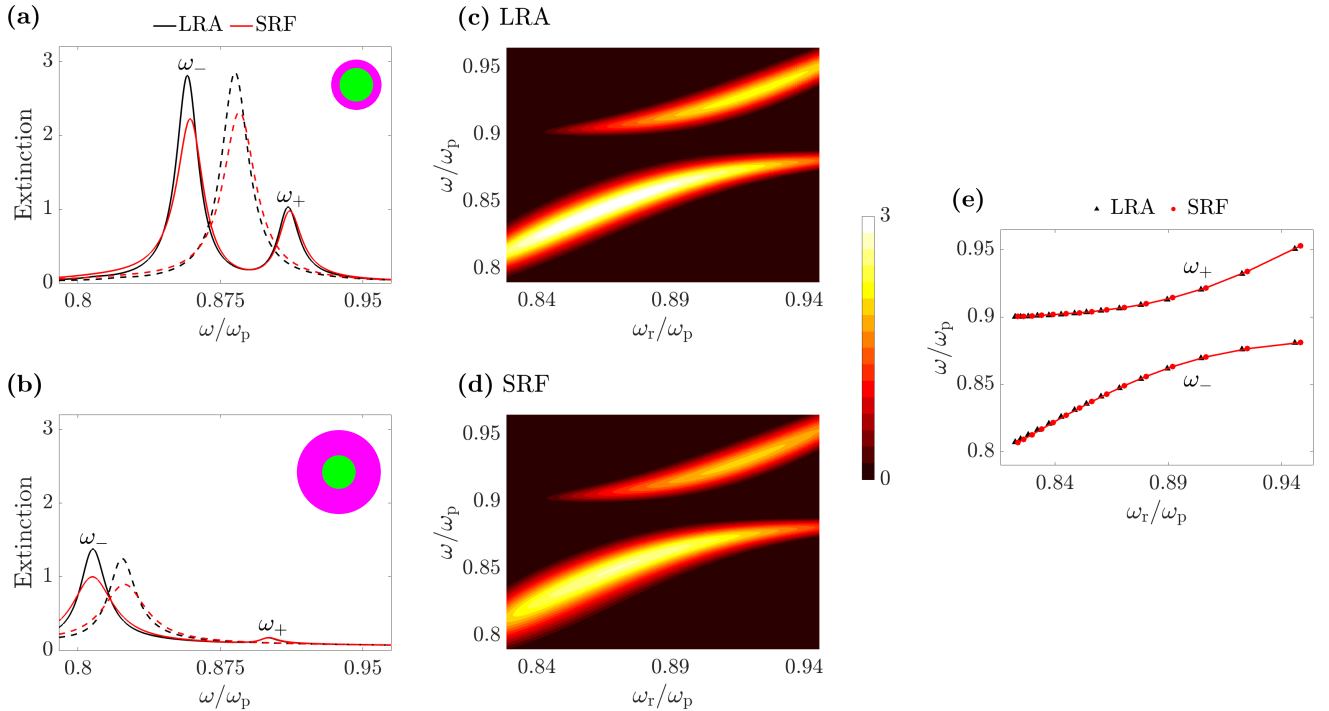


FIG. 4. (a, b) Extinction cross sections, normalized to the geometric cross section πR^2 , for a sodium shell of width (a) 3.14 nm and (b) 13.0 nm around an excitonic core with a 5 nm radius. The hybrid modes ω_{\pm} for SRF (LRA) are shown as the solid red (black) lines. The dashed red (black) lines are the extinction cross section of the sodium shell within SRF (LRA) with an air core instead. (c, d) Logarithmically scaled extinction contour maps as a function of resonance frequency ω_r for (c) LRA and (d) SRF, sharing a common color scale. (e) Hybrid mode resonance energies, shown as red dots (black triangles) within SRF (LRA), as a function of the sodium shell resonance energy. The red lines show the trend of the resonance frequencies of SRF for both hybrid modes.

larger shell widths, such as the one shown in Fig. 4b with an overall redshift of the lower mode, the correction to the NP mode becomes the more significant contribution.

To compare the mode splitting quantitatively, we consider both models at zero detuning, i.e. when the cavity mode of the sodium shell in the absence of the excitonic core has resonance frequency ω_r that equals the excitonic frequency ω_{exc} . The tuning of the energy is done by varying the width of the sodium shell while keeping the inner radius constant. Zero detuning occurs for the LRA shell, seen in Fig. 4a at width $W = 3.14$ nm, where the difference in energy between the resonance peaks is 312 meV. For SRF, zero detuning occurs at a slightly larger width $W = 3.26$ nm with a difference in energy of 314 meV. Comparing the two values, it is apparent that the energy difference between the corresponding coupling strengths is negligible.

Focusing on the coupled cavity mode across the entire resonance frequency spectrum, Figs. 4c and d show the contour maps of the extinction cross section for LRA and SRF, respectively, as a function of the plasmonic resonance frequency ω_r/ω_p of the uncoupled cavity mode. The plasmonic resonance energy is calculated as the resonance of the cavity mode of the sodium shell in the absence of the excitonic core for a varying shell width W

and a fixed inner radius $R_1 = 5$ nm, and the shell width W varies from 1 to 15 nm. On both panels, it can be seen that the splitting is centred around the excitonic energy $\omega_{\text{exc}}/\omega_p \simeq 0.88$, as expected. Comparing Figs. 4c and d, the most notable difference is the broadening of the hybrid modes in SRF compared to LRA due to Landau damping, especially for the lower mode. Otherwise, the hybrid modes are still discernible in the strong coupling regime.

To better visualize the splitting in the SRF and LRA models, Fig. 4e shows the resonance energies of the hybrid modes of select plasmonic resonance energies ω_r . We see that, compared to the energy difference between the hybrid modes, the prior described shifts of the SRF modes from the LRA modes become negligible. This means that the energy split between the hybrid modes is practically not affected by nonlocality for all the shown plasmonic resonance energies.

III. CONCLUSION

We examined the optical response of different core-shell configurations of plasmonic-excitonic composites and compared the results obtained with standard LRA

to those produced with a nonlocal surface-response approach. Specifically, we chose to work within the Feibelman framework, which is ideal for describing the spill-out in alkali metals, together with surface-enabled Landau damping. Even though energy shifts and resonance broadenings of the hybrid modes are evident in the spectra, both models generate very similar anticrossings in all configurations, since both hybrid modes shift within SRF by the same amount. We thus found that LRA provides a reliable estimation of the coupling strength, even when the dimensions of metallic–excitonic systems are driven down to the limits of nanofabrication capabilities.

ACKNOWLEDGMENTS

We acknowledge funding from VILLUM Fonden (Villum Investigator, N. A. Mortensen, grant No. 16498). The Center for Polariton-driven Light–Matter Interactions (POLIMA) is sponsored by the Danish National Research Foundation (Project No. DNR165).

APPENDIX

Mie theory is used throughout this paper to calculate extinction cross-sections and predict the optical response of the spherical NPs presented. The coefficients and equations for the cross sections that we have used are presented in this appendix. For all materials modelled, the relative permeability is always assumed $\mu = 1$.

For a spherical NP with permittivity ε_1 and permeability μ_1 embedded in a host medium with permittivity ε_2 and permeability μ_2 , the scattering Mie coefficients using an LRA framework are [63, 64]

$$T_{E\ell} = \frac{j_\ell(x_{11})\Psi'_\ell(x_{21})\varepsilon_1 - j_\ell(x_{21})\Psi'_\ell(x_{11})\varepsilon_2}{h_\ell^{(1)}(x_{21})\Psi'_\ell(x_{11})\varepsilon_2 - j_\ell(x_{11})\xi'_\ell(x_{21})\varepsilon_1} \quad (7)$$

$$T_{H\ell} = \frac{j_\ell(x_{11})\Psi'_\ell(x_{21})\mu_1 - j_\ell(x_{21})\Psi'_\ell(x_{11})\mu_2}{h_\ell^{(1)}(x_{21})\Psi'_\ell(x_{11})\mu_2 - j_\ell(x_{11})\xi'_\ell(x_{21})\mu_1}, \quad (8)$$

where $x_{i1} = k_i R_1$ for wavenumbers k_1 and k_2 of the core and host material, respectively. The functions $\Psi'_\ell(z)$ and $\xi'_\ell(z)$ are the derivatives with respect to their argument z of the Ricatti-Bessel functions $\Psi_\ell(z) = zj_\ell(z)$ and $\xi_\ell(z) = zh_\ell^{(1)}(z)$, where $j_\ell(z)$ and $h_\ell^{(1)}(z) = j_\ell(z) + iy_\ell(z)$ are the spherical Bessel functions and spherical Hankel functions of the first kind, respectively (with $y_\ell(z)$ being the spherical Bessel function of the second kind, a.k.a. Neumann function).

We now introduce the Feibelman correction to a spherical NP of plasmonic material. The scattering Mie coef-

ficients in this SRF framework become [31]

$$T_{E\ell} = \frac{C_{E\ell}^n + \bar{\varepsilon}[\bar{d}_\perp j_\ell(x_{21})j_\ell(x_{11}) + \bar{d}_\parallel \Psi'_\ell(x_{21})\Psi'_\ell(x_{11})]}{C_{E\ell}^d - \bar{\varepsilon}[\bar{d}_\perp h_\ell^{(1)}(x_{21})j_\ell(x_{11}) + \bar{d}_\parallel \xi'_\ell(x_{21})\Psi'_\ell(x_{11})]} \quad (9)$$

$$T_{H\ell} = \frac{C_{H\ell}^n + [\mu_2 x_{11}^2 - \mu_1 x_{21}^2] \bar{d}_\parallel j_\ell(x_{21})j_\ell(x_{11})}{C_{H\ell}^d - [\mu_2 x_{11}^2 - \mu_1 x_{21}^2] \bar{d}_\parallel h_\ell^{(1)}(x_{21})j_\ell(x_{11})}, \quad (10)$$

where $\bar{\varepsilon} = \varepsilon_1 - \varepsilon_2$, $\bar{d}_\perp = \ell(\ell + 1)d_\perp/R_1$ and $\bar{d}_\parallel = d_\parallel/R_1$. The coefficients $C_{P\ell}^n$ and $C_{P\ell}^d$ are the numerator and denominator from Eqs. (7) and (8),

$$C_{P\ell}^n = j_\ell(x_{11})\Psi'_\ell(x_{21})p_1 - j_\ell(x_{21})\Psi'_\ell(x_{11})p_2$$

$$C_{P\ell}^d = h_\ell^{(1)}(x_{21})\Psi'_\ell(x_{11})p_2 - j_\ell(x_{11})\xi'_\ell(x_{21})p_1,$$

where $p_m = \varepsilon_m$ if $P = E$ and $p_m = \mu_m$ if $P = H$. Note that if $d_{\perp,\parallel} = 0$, the equations will become identical to Eqs. (7) and (8).

We further add an excitonic shell to our plasmonic core NP; for a configuration with a non-plasmonic shell the scattering Mie-coefficients become

$$T_{E\ell} = \frac{[\Psi'_\ell(x_{32})h_\ell^{(1)}(x_{22})\varepsilon_2 - j_\ell(x_{32})\xi'_\ell(x_{22})\varepsilon_3]T'_{E\ell} + S_{E\ell}^n}{[h_\ell^{(1)}(x_{32})\xi'_\ell(x_{22})\varepsilon_3 - \xi'_\ell(x_{32})h_\ell(x_{22})\varepsilon_2]T'_{E\ell} + S_{E\ell}^d} \quad (11)$$

$$T_{H\ell} = \frac{[\Psi'_\ell(x_{32})h_\ell^{(1)}(x_{22})\mu_2 - j_\ell(x_{32})\xi'_\ell(x_{22})\mu_3]T'_{H\ell} + S_{H\ell}^n}{[h_\ell^{(1)}(x_{32})\xi'_\ell(x_{22})\mu_3 - \xi'_\ell(x_{32})h_\ell(x_{22})\mu_2]T'_{H\ell} + S_{H\ell}^d}, \quad (12)$$

where the arguments $x_{i2} = k_i R$, are in terms of the outer radius $R = R_1 + W$ and the wavenumbers k_2 and k_3 in the excitonic shell and host medium, air, respectively. $T'_{P\ell}$ for polarization $P = E, H$ are the Mie coefficients for the core, using (7) and (8) for LRA and (9) and (10) for an SRF core. The coefficients $S_{P\ell}^n$ and $S_{P\ell}^d$ are given by

$$S_{P\ell}^n = \Psi'_\ell(x_{32})j_\ell(x_{22})p_2 - j_\ell(x_{32})\Psi'_\ell(x_{22})p_3$$

$$S_{P\ell}^d = h_\ell^{(1)}(x_{32})\Psi'_\ell(x_{22})p_3 - \xi'_\ell(x_{32})j_\ell(x_{22})p_2,$$

where $p_m = \varepsilon_m$ if $P = E$ and $p_m = \mu_m$ if $P = H$. These coefficients are the LRA Mie coefficients evaluated at the shell-host boundary.

Inverting the geometry such that we have a non-plasmonic core and a plasmonic shell, the scattering Mie coefficients become

$$T_{E\ell} = \frac{K_{E\ell}^n + S_{E\ell}^n + (\varepsilon_2 - \varepsilon_3)(D_{E\ell}^n + N_{E\ell}^n)}{K_{E\ell}^d + S_{E\ell}^d - (\varepsilon_2 - \varepsilon_3)(D_{E\ell}^d + N_{E\ell}^d)} \quad (13)$$

$$T_{H\ell} = \frac{K_{H\ell}^n + S_{H\ell}^n + (x_{22}^2 \mu_3 - x_{32}^2 \mu_2)(D_{H\ell}^n + N_{H\ell}^n)}{K_{H\ell}^d + S_{H\ell}^d - (x_{22}^2 \mu_3 - x_{32}^2 \mu_2)(D_{H\ell}^d + N_{H\ell}^d)}, \quad (14)$$

where the coefficients $N_{P\ell}^{n,d}$ are

$$\begin{aligned} N_{E\ell}^n &= [\bar{d}_\perp h_\ell^{(1)}(x_{22})h_\ell^{(1)}(x_{32}) + \bar{d}_\parallel \xi'_\ell(x_{22})\xi'_\ell(x_{32})]T'_{E\ell} \\ N_{E\ell}^d &= [\bar{d}_\perp h_\ell^{(1)}(x_{22})h_\ell^{(1)}(x_{32}) + \bar{d}_\parallel \xi'_\ell(x_{22})\xi'_\ell(x_{32})]T'_{E\ell} \\ N_{H\ell}^n &= \bar{d}_\parallel h_\ell^{(1)}(x_{22})j_\ell(x_{32})T'_{H\ell} \\ N_{H\ell}^d &= \bar{d}_\parallel h_\ell^{(1)}(x_{22})h_\ell^{(1)}(x_{32})T'_{H\ell} \end{aligned}$$

We further introduce the coefficients $D_{P\ell}^{n,d}$ as

$$\begin{aligned} D_{E\ell}^n &= [\bar{d}_\perp j_\ell(x_{22})j_\ell(x_{32}) + \bar{d}_\parallel \Psi'_\ell(x_{22})\Psi'_\ell(x_{32})] \\ D_{E\ell}^d &= [\bar{d}_\perp j_\ell(x_{22})h_\ell^{(1)}(x_{32}) + \bar{d}_\parallel \Psi'_\ell(x_{22})\xi'_\ell(x_{32})] \\ D_{H\ell}^n &= \bar{d}_\parallel j_\ell(x_{22})j_\ell(x_{32}) \\ D_{H\ell}^d &= \bar{d}_\parallel j_\ell(x_{22})h_\ell^{(1)}(x_{32}), \end{aligned}$$

which are terms also shown in (9) and (10), they represent a similar correction to the shell–host boundary as previously considered for the core–host boundary. Lastly,

we introduce the $K_{P\ell}^{n,d}$ coefficients

$$\begin{aligned} K_{P\ell}^n &= [\Psi'_\ell(x_{32})h_\ell^{(1)}(x_{22})p_2 - j_\ell(x_{32})\xi'_\ell(x_{22})p_3]T'_{P\ell} \\ K_{P\ell}^d &= [h_\ell(x_{32})\xi'_\ell(x_{22})p_3 - \xi'_\ell(x_{32})h_\ell^{(1)}(x_{22})p_2]T'_{P\ell}, \end{aligned}$$

which are recognisable from (11) and (12) for the core–shell NP with non-plasmonic shell. Note that if $d_{\parallel,\perp} = 0$ the equations will become identical to (11) and (12).

The scattering σ_{sc} , absorption σ_{abs} and extinction σ_{ext} cross-sections for spherical NPs are calculated using Mie coefficients according to the following equations

$$\sigma_{\text{sc}} = \frac{2}{(kR)^2} \sum_{\ell=1}^{\infty} (2\ell + 1) (|T_{E\ell}|^2 + |T_{H\ell}|^2) \quad (15)$$

$$\sigma_{\text{ext}} = -\frac{2}{(kR)^2} \sum_{\ell=1}^{\infty} (2\ell + 1) \text{Re}(T_{E\ell} + T_{H\ell}) \quad (16)$$

$$\sigma_{\text{abs}} = \sigma_{\text{ext}} - \sigma_{\text{sc}}, \quad (17)$$

where R is the outer radius, k the wave vector of the host medium and $T_{E\ell}$ and $T_{H\ell}$ are the scattering Mie coefficients for the electric and magnetic multipoles, respectively.

* ct@mci.sdu.dk

- [1] D. Pines and D. Bohm, A collective description of electron interactions: II. Collective vs individual particle aspects of the interactions, *Phys. Rev.* **85**, 338 (1952).
- [2] R. H. Ritchie, Plasma losses by fast electrons in thin films, *Phys. Rev.* **106**, 874 (1957).
- [3] E. N. Economou, Surface plasmons in thin films, *Phys. Rev.* **182**, 539 (1969).
- [4] Y.-Y. Teng and E. A. Stern, Plasma radiation from metal grating surfaces, *Phys. Rev. Lett.* **19**, 511 (1967).
- [5] R. F. Oulton, G. Bartal, D. F. P. Pile, and X. Zhang, Confinement and propagation characteristics of subwavelength plasmonic modes, *New Journal of Physics* **10**, 105018 (2008).
- [6] R. de Waele, A. F. Koenderink, and A. Polman, Tunable nanoscale localization of energy on plasmon particle arrays, *Nano Letters* **7**, 2004 (2007).
- [7] S. Pillai, K. R. Catchpole, T. Trupke, and M. A. Green, Surface plasmon enhanced silicon solar cells, *Journal of Applied Physics* **101**, 093105 (2007).
- [8] K. A. Willets and R. P. Van Duyne, Localized surface plasmon resonance spectroscopy and sensing, *Annu. Rev. Phys. Chem.* **58**, 267 (2007).
- [9] J. D. Jackson, *Classical Electrodynamics*, 3rd ed. (Wiley, 1998).
- [10] N. W. Ashcroft and N. D. Mermin, *Solid State Physics* (Harcourt, Orlando, 1976).
- [11] C. Tserkezis, *Towards quantum nanophotonics: from quantum-informed plasmonics to strong coupling* (2021), dr. Techn. thesis (University of Southern Denmark).
- [12] M. S. Tame, K. R. McEnery, Ş. K. Özdemir, J. Lee, S. A. Maier, and M. S. Kim, Quantum plasmonics, *Nature Physics* **9**, 329 (2013).
- [13] N. A. Mortensen, Mesoscopic electrodynamics at metal surfaces, *Nanophotonics* **10**, 2563 (2021).
- [14] U. Hohenester, *Nano and Quantum Optics: An Introduction to L* (Springer, 2020).
- [15] X. Li, D. Xiao, and Z. Zhang, Landau damping of quantum plasmons in metal nanostructures, *New Journal of Physics* **15**, 023011 (2013).
- [16] P. E. Stamatopoulou and C. Tserkezis, Finite-size and quantum effects in plasmonics: manifestations and theoretical modelling, *Opt. Mater. Express* **12**, 1869 (2022).
- [17] U. Kreibig and M. Vollmer, *Optical Properties of Metal Clusters* (Springer, 1995).
- [18] R. Ruppin, Optical properties of a plasma sphere, *Phys. Rev. Lett.* **31**, 1434 (1973).
- [19] G. Barton, Some surface effects in the hydrodynamic model of metals, *Rep. Prog. Phys.* **42**, 963 (1979).
- [20] F. J. García de Abajo, Nonlocal effects in the plasmons of strongly interacting nanoparticles, dimers, and waveguides, *J. Phys. Chem. C* **112**, 17983 (2008).
- [21] N. A. Mortensen, S. Raza, M. Wubs, T. Søndergaard, and S. I. Bozhevolnyi, A generalized non-local optical response theory for plasmonic nanostructures, *Nature Communications* **5**, 3809 (2014).
- [22] A. R. Melnyk and M. J. Harrison, Theory of optical excitation of plasmons in metals, *Phys. Rev. B* **2**, 835 (1970).
- [23] S. Raza, G. Toscano, A.-P. Jauho, M. Wubs, and N. A. Mortensen, Nonlocal resonances in nanoplasmonic structures due to nonlocal response, *Phys. Rev. B* **84**, 121412 (2011).
- [24] G. Toscano, J. Straubel, A. Kwiatkowski, C. Rockstuhl, F. Evers, H. Xu, N. A. Mortensen, and M. Wubs, Resonance shifts and spill-out effects

- in self-consistent hydrodynamic nanoplasmonics, *Nature Communications* **6**, 7132 (2015).
- [25] W. Yan, Hydrodynamic theory for quantum plasmonics: linear-response dynamics of the inhomogeneous electron gas, *Phys. Rev. B* **91**, 115416 (2015).
- [26] C. Ciraci and F. Della Sala, Quantum hydrodynamic theory for plasmonics: Impact of the electron density tail, *Phys. Rev. B* **93**, 205405 (2016).
- [27] G. Weick, G.-L. Ingold, R. A. Jalabert, and D. Weinmann, Surface plasmon in metallic nanoparticles: Renormalization effects due to electron-hole excitations, *Phys. Rev. B* **74**, 165421 (2006).
- [28] L. Stella, P. Zhang, F. J. García-Vidal, A. Rubio, and P. García-González, Performance of nonlocal optics when applied to plasmonic nanostructures, *J. Phys. Chem. C* **117**, 8941 (2013).
- [29] T. V. Teperik, P. Nordlander, J. Aizpurua, and A. G. Borisov, Quantum effects and nonlocality in strongly coupled plasmonic nanowire dimers, *Opt. Express* **21**, 27306 (2013).
- [30] P. J. Feibelman, Surface electromagnetic fields, *Progress in Surface Science* **12**, 287 (1982).
- [31] P. A. D. Gonçalves, T. Christensen, N. Rivera, A.-P. Jauho, N. A. Mortensen, and M. Soljačić, Plasmon-emitter interactions at the nanoscale, *Nature Communications* **11**, 366 (2020).
- [32] T. Christensen, W. Yan, A.-P. Jauho, M. Soljačić, and N. A. Mortensen, Quantum corrections in nanoplasmonics: Shape, scale, and material, *Phys. Rev. Lett.* **118**, 157402 (2017).
- [33] J. T. Hugall, A. Singh, and N. F. van Hulst, Plasmonic cavity coupling, *ACS Photonics* **5**, 43 (2018).
- [34] O. Bitton, S. N. Gupta, and G. Haran, Quantum dot plasmonics: from weak to strong coupling, *Nanophotonics* **8**, 559 (2019).
- [35] S. Balci, E. Karademir, C. Kocabas, and A. Aydinli, Absorption enhancement of molecules in the weak plasmon-exciton coupling regime, *Opt. Lett.* **39**, 4994 (2014).
- [36] J. Lee, A. O. Govorov, J. Dulka, and N. A. Kotov, Bioconjugates of CdTe nanowires and Au nanoparticles: Plasmon-exciton interactions, luminescence enhancement, and collective effects, *Nano Letters* **4**, 2323 (2004).
- [37] A. Kumar, R. Srivastava, P. Tyagi, D. Mehta, and M. Kamalasanan, Efficiency enhancement of organic light emitting diode via surface energy transfer between exciton and surface plasmon, *Organic Electronics* **13**, 159 (2012).
- [38] A. F. Koenderink, On the use of Purcell factors for plasmon antennas, *Opt. Lett.* **35**, 4208 (2010).
- [39] C. Tserkezis, A. I. Fernández-Domínguez, P. A. D. Gonçalves, F. Todisco, J. D. Cox, K. Busch, N. Stenger, S. I. Bozhevolnyi, N. A. Mortensen, and C. Wolff, On the applicability of quantum-optical concepts in strong-coupling nanophotonics, *Rep. Prog. Phys.* **83**, 082401 (2020).
- [40] P. Törmä and W. L. Barnes, Strong coupling between surface plasmon polaritons and emitters: a review, *Rep. Prog. Phys.* **78**, 013901 (2014).
- [41] Q. Zhao, W.-J. Zhou, Y.-H. Deng, Y.-Q. Zheng, Z.-H. Shi, L. K. Ang, Z.-K. Zhou, and L. Wu, Plexcitonic strong coupling: unique features, applications, and challenges, *J. Phys. D: Appl. Phys.* **55**, 203002 (2022).
- [42] G. Zengin, M. Wersäll, S. Nilsson, T. J. Antosiewicz, M. Käll, and T. Shegai, Realizing strong light-matter interactions between single-nanoparticle plasmons and molecular excitons at ambient conditions, *Phys. Rev. Lett.* **114**, 157401 (2015).
- [43] B. D. Gates, Q. Xu, M. Stewart, D. Ryan, C. G. Willson, and G. M. Whitesides, New approaches to nanofabrication: Molding, printing, and other techniques, *Chemical Reviews* **105**, 1171 (2005).
- [44] J. Bellessa, C. Bonnard, J. C. Plenet, and J. Mugnier, Strong coupling between surface plasmons and excitons in an organic semiconductor, *Phys. Rev. Lett.* **93**, 036404 (2004).
- [45] R. Chikkaraddy, B. de Nijs, F. Benz, S. J. Barrow, O. A. Scherman, E. Rosta, A. Demetriadou, P. Fox, O. Hess, and J. J. Baumberg, Single-molecule strong coupling at room temperature in plasmonic nanocavities, *Nature* **535**, 127 (2016).
- [46] M. Stührenberg, S. Munkhbat, D. G. Baranov, J. Cuadra, A. B. Yankovich, T. J. Antosiewicz, E. Olsson, and T. Shegai, Strong light-matter coupling between plasmons in individual gold bipyramids and excitons in mono- and multilayer WSe₂, *Nano Lett.* **18**, 5938 (2019).
- [47] M. Geisler, X. Cui, J. Wang, T. Rindzevicius, L. Gammelgaard, B. S. Jessen, P. A. D. Gonçalves, F. Todisco, P. Bøggild, A. Boisen, M. Wubs, N. A. Mortensen, S. Xiao, and N. Stenger, Single-crystalline gold nanodisks on WS₂ mono- and multilayers for strong coupling at room temperature, *ACS Photonics* **6**, 994 (2019).
- [48] P. A. Hobson, W. L. Barnes, D. G. Lidzey, G. A. Gehring, D. M. Whittaker, M. S. Skolnick, and S. Walker, Strong exciton-photon coupling in a low-Q all-metal mirror microcavity, *Applied Physics Letters* **81**, 3519 (2002).
- [49] J. Bellessa, C. Symonds, K. Vynck, A. Lemaitre, A. Brioude, L. Beaur, J. C. Plenet, P. Viste, D. Felbacq, E. Cambril, and P. Valvin, Giant Rabi splitting between localized mixed plasmon-exciton states in a two-dimensional array of nanosize metallic disks in an organic semiconductor, *Phys. Rev. B* **80**, 033303 (2009).
- [50] C. Tserkezis, M. Wubs, and N. A. Mortensen, Robustness of the Rabi splitting under nonlocal corrections in plexcitonics, *ACS Photonics* **5**, 133 (2018).
- [51] W. Ekardt, Dynamical polarizability of small metal particles: Self-consistent spherical jellium background model, *Phys. Rev. Lett.* **52**, 1925 (1984).
- [52] E. Townsend and G. W. Bryant, Plasmonic properties of metallic nanoparticles: The effects of size quantization, *Nano Letters* **12**, 429 (2012).
- [53] J. Zuloaga, E. Prodan, and P. Nordlander, Quantum plasmonics: optical properties and tunability of metallic nanorods, *ACS Nano* **4**, 5269 (2010).
- [54] J. Zuloaga, E. Prodan, and P. Nordlander, Quantum description of the plasmon resonances of a nanoparticle dimer, *Nano Lett.* **9**, 887 (2009).
- [55] T. V. Teperik, P. Nordlander, J. Aizpurua, and A. G. Borisov, Robust subnanometric plasmon ruler by rescaling of the nonlocal optical response, *Phys. Rev. Lett.* **110**, 263901 (2013).
- [56] G. Mie, Beiträge zur Optik trüber Medien, speziell kolloidaler Metallösungen, *Ann. Phys.* **330**, 377 (1908).
- [57] A. Babaze, E. Ogando, P. E. Stamatopoulou, C. Tserkezis, N. A. Mortensen, J. Aizpurua, A. G. Borisov, and R. Esteban, Quantum surface effects in the electromagnetic coupling between a quantum emitter and a plasmonic nanoantenna: time-dependent density

- functional theory vs. semiclassical feibelman approach, *Opt. Express* **30**, 21159 (2022).
- [58] A. Babaze, T. Neuman, R. Esteban, J. Aizpurua, and A. G. Borisov, Dispersive surface-response formalism to address nonlocality in extreme plasmonic field confinement, *Nanophotonics* **12**, 3277 (2023).
- [59] W. Yan, M. Wubs, and N. Asger Mortensen, Projected dipole model for quantum plasmonics, *Phys. Rev. Lett.* **115**, 137403 (2015).
- [60] N. T. Fofang, T.-H. Park, O. Neumann, N. A. Mirin, P. Nordlander, and N. J. Halas, Plexcitonic nanoparticles: Plasmon-exciton coupling in nanoshell-J-aggregate complexes, *Nano Letters* **8**, 3481 (2008).
- [61] T. J. Antosiewicz, S. P. Apell, and T. Shegai, Plasmon–exciton interactions in a core–shell geometry: From enhanced absorption to strong coupling, *ACS Photonics* **1**, 454 (2014).
- [62] C. Tserkezis, G. Gantzounis, and N. Stefanou, Collective plasmonic modes in ordered assemblies of metallic nanoshells, *J. Phys. Condens. Matter* **20**, 075232 (2008).
- [63] C. F. Bohren and D. R. Huffman, *Absorption and Scattering of Light by Small Particles* (Wiley, 1983).
- [64] M. Born and E. Wolf, *Principles of Optics: Electromagnetic Theory of Propagation, In* 7th ed. (Cambridge University Press, 1999).